ABSTRACT

Title of Thesis: FDS SIMULATIONS OF THE TRANSPORT OF COLD FIREBRANDS IN WIND TUNNEL EXPERIMENTS

Xinyu Fan, Master of Science, 2020

Thesis Directed By: Professor Arnaud Trouve
Department of fire protection engineering

In wildland fires, the transport of firebrands is the main reason causing subsequent spot fires. The embers can travel farther than the fire itself and ignite the houses at the wildland urban interface (WUI). We consider previous experiments performed in a wind tunnel and used to characterize the transport of cold particles in a controlled velocity field that corresponds to a turbulent jet in a cross-flow. We perform numerical simulations of these experiments using the Fire Dynamics Simulator (FDS). The simulated jet and cross-wind velocity field are adjusted and tested to match the flow velocities measured in the experiments. The solid particles are simulated using the FDS Lagrangian model and our study includes comparisons between simulated and measured trajectories. The relationship between the particle flying pattern with the wind velocity field is examined.

FDS SIMULATIONS OF THE TRANSPORT OF COLD FIREBRANDS IN WIND TUNNEL EXPERIMENTS

by

Xinyu Fan

Thesis submitted to the Faculty of the Graduate School of the
University of Maryland, College Park, in partial fulfillment
of the requirements for the degree of
Master of Science
2020

Advisory Committee:
Professor Arnaud Trouvé, Chair
Professor Peter Sunderland
Professor Stanislav Stoliarov

Acknowledgements

First, I would also like to thank my parents for their support and their continuous demonstration of the importance of hard work and being passionate by living out those values every day. I am extremely privileged to have got these values all along the completion of my thesis.

Next, I would like to sincerely thank my advisor, Dr. Arnaud Trouvé. Your work ethic and your serious attitude for academic study are unrivaled, which inspired me a lot to make progress in my research. I greatly appreciate your wisdom to pick up the research topic about wildland fires and FDS for my graduate study. This is a great topic combined both the fundamental science and applied engineering, I really enjoyed my time doing the simulations and exploring more truth about wildland fires. Thank you for coordinating with other universities internationally and bringing other researchers to our group, it is really inspiring to have teammates to work on the same projects and share thoughts together.

I would like to thank the other members in my research group. Thank you for supporting me and accompany me with this academic journey. Thank you Dr. Salman to get me start with deepthought2. You help me start running my FDS input files using multiple processors and that saved me a lot of time. Thank you Mohamed for mentoring me about the turbulence and fluid dynamic knowledge and keep encouraging me I can make it someday. Thank you Rui for answering and discussing the problems I came across in my research and courses with me. It inspired me a lot and let me have a better understanding for my research and my course. Thank you Yiren and Leo for working on

the same projects with me, we shared and talked our progress together, and I learned a lot from you.

I would like to thank all of the committee members who have generously given their time to provide critical feedback to my research. My advisory committee consisted of Dr. Peter Sunderland and Dr. Stanislav. Stoliarov. Thank you for the comments and questions that have strengthened the outcome of this research. Last but not the least, I would like to thank the FPE department at University of Maryland. Thank you for providing the helpful courses for the fire science study, NFPA standard learning and how to use engineering software. I would like to extend my sincere esteems to all staffs working in FPE department for their guide and support.

Table of Contents

Chapter 1: Introduction

1.1 Background

In the past years, there have been lots of wildland fires happening all over the world. Wildfires threaten the life safety of the people living in the wildland urban interface (WUI) and cause hundreds of millions of properties loss. Climate change has a series of impacts related to wildland fires: higher temperatures, more frequent droughts and changes in raining patterns. The damage of the wildland fire shows its potential to become more serious with time. Today, the fire season is 78 days longer than the fire season in the 1970s. Starting in the 21th century, 10 states in America have seen their biggest fire in recorded history. Every year around 40,000 to 50,000 wildland fires break out [1]. Some of them are just the harmless natural process and even benefit the soil by accumulating more nutrition for it. Urban areas continue to develop their boundary to forest and wildland causing the WUI area to become bigger, making wildland fires a bigger issue today.

When a wildland fire starts in the middle of a forest or any other vegetation-covered area which is far away from a WUI, the effective ways to fight the fire are to slow down the rate of spread. By dividing large fires into a few small fires, using barriers, and putting out the small fires one at a time, the large fires can get controlled. Wind is an important and dangerous factor in wildland fires. For example, the Thomas fire broke out near in 2017 near Ventura and Santa Barbara counties in California. This fire took over $204 million to fight and caused over $2.2 billion in damage. This severe wildland fire took 2 months to put out. One of the major factors that made this fire so destructive was the Santa Ana winds, which are strong, extremely dry winds that happen in winter and blow towards

the ocean. The wind not only increases the rate of spread of the flames on the fireline, it also blows the firebrands generated from the fire. The presence of a firebrand shower provides a new mechanism for fire spread. In the wildland, firebrands land on plants far away from the fireline and it causes spot ignition which develops as a secondary fire and interacts with the main fire. In the WUI area, the firebrands may land on roofs of houses or ignite plants in the yard which threaten life safety directly. Past observations have documented how the transport of firebrands causes fire spread and threaten people's lives in London [2], Tokyo [3], Australia [4] and, so on.

Fernandez-Pello has analyzed how spot fires happened in WUI fires [5]. He summarized the state of the wildfire spotting problems by introducing every individual process in this spotting problem: the generation of the particles, their flight by lofting and wind drag, their thermochemical state, and the onset of ignition after they land. This study gives a comprehensive understanding of the wildland spot fire ignition process and provides information on how the firebrands travel in actual wildland fires. Fernandez-Pello has also done research comparing the flight paths of burning embers produced by the collision of high voltage power lines with surrounding trees and flight paths of hot metal particles. The data has been analyzed by plotting out the particle trajectories. The results show that in the same wind velocity field, firebrands have the greater travelling distances when compared to metal particles. This is proof of how far the firebrands can fly and why it's important to study them [6].

Past firebrand investigations have not been able to quantify the vulnerabilities of structures to ignition from firebrand showers. To address this problem, Manzello has done experiments on firebrands attacking structures, which simulate conditions found in actual

WUI fires. He developed the NIST Firebrand Generator, also referred to as the NIST Dragon [7]. This study explains how firebrands travel and after they land, how they accumulate and flaming ignition happens. The FDS Dragon input files provided as example files with the installation of FDS illustrate how to introduce particles to velocity fields in FDS simulation, which helps with the setup of the FDS input file for this paper. To get more data about the size and mass of the firebrands, Manzello has done a series of real-scale experiments. The experiment analyzes different types of vegetation at different moisture levels. The Douglas-fir trees and Korean pine trees were burnt at different moisture levels and their firebrands collected and measured. The mass and size distribution of firebrands generated from his experiment are useful for fire models used to predict spotting in wildland fires [8] [9].

Manzello, Suzuki and Gollner have been studying the role of firebrand mechanisms on large outdoor fire spread and how the firebrands result in severe large outdoor fires [10]. This study clarifies the process of how firebrands spread and cause WUI fires with the actual life wildland fire examples in Japan. Caton, Hakes and Gollner have done research on the pathways for fire spread in the WUI and on fire exposure conditions as well as the response and mitigation strategies with lots of case studies, such as Waldo Canyon Fire, Witch Creek and Guejito Fires and Grass Valley Fire and so on [11] [12]. The study of these past wildfires helps us understand how fire spread in the wildland and shows that ember ignition is one of the pathways of fire spread. The information collected in these studies help us in the design of a firebrand transport model to simulate actual wildland fires. The model of particle transport presented in this manuscript simulates solid particles that are representative of embers found in wildfire applications. The embers considered

here are cold and chemically inert. Future work will consider an extension to the case of burning embers under flaming or smoldering conditions.

1.2 Review of the Eulerian-Lagrangian Framework

In the process of a typical firebrand shower there are several phases. When a fire breaks out in the wildland, plants on fire or heated up by the nearby flames can experience damage to their vegetative structure. This thermo-mechanical process causes the burned plants to break off and to release small lightweight solid particles called firebrands. After these firebrands are released in the environment, the fire plume lofts them. The buoyancy and upward velocity of the plume convect the firebrands vertically, the atmospheric wind convects the firebrands horizontally. Within the atmospheric boundary layer, the downwind and lofting transport happen together. Tohidi and Kaye have studied firebrand transport in a simplified configuration [13]. There are lots of factors that impact the fire plume, such as the topography, fuel breaks and, so on. Therefore, the firebrands lofting velocity field can have multiple values. Just like the lofting velocity field, the atmospheric wind can change from time to time and there can be multiple combinations of these flow velocity fields. After the firebrands have been lofted and blown downwind, they may land somewhere else ahead of the fireline, and ignite plants or roofs that they land on.

Here in this paper, FDS is used to simulate Tohidi and Kaye's particle experiment in the wind tunnel. FDS is a computational fluid dynamics (CFD) model for simulating fire-driven flow. Because it is concentrated on simulating fires and fire-driven flow, this software can solve numerically the Navier-Stokes equations for low-speed, thermally-driven flow by grid. FDS can simulate the pyrolysis process and calculate transferred heat. The results can be viewed in the output Smokeview video; the movement of the smoke,

fire spreading and particles transport. FDS can also provide the numerical output data for the claimed specific locations in the simulation domain. For particle transport, FDS uses the following equations to simulate the process.

The gas phase equations are solved in an Eulerian framework while the solid firebrand equations are solved in a Lagrangian framework. The firebrands are affected by gravity in the z direction and will ultimately land on the ground. Here is the expression for total drag force for n particles in atmospheric wind:

$$F = \frac{1}{2} C_D \rho_g A_{p,c} \left[\left(u_{g,j} - u_{p,j}\right)\left(u_{g,j} - u_{p,j}\right) \right]^{\frac{1}{2}} \left(u_{p,1} - u_{g,1}\right) \quad (1)$$

where C_D is the drag coefficient. ρ_g is the density of the gas. $A_{p,c}$ is the particle cross-sectional area. $u_{g,j}$ is the ambient wind velocity. $u_{p,j}$ is the particle velocity.

The firebrands here are not massless particles and their acceleration can be generated from the momentum equation. The velocity equations in the three spatial directions for the firebrands are as follows:

$$\frac{du_{p,1}}{dt} = \frac{C_D \rho_g A_{p,c} \left[\left(u_{g,j} - u_{p,j}\right)\left(u_{g,j} - u_{p,j}\right) \right]^{\frac{1}{2}} (u_{p,1} - u_{g,1})}{2m_p} \quad (2)$$

$$\frac{du_{p,2}}{dt} = \frac{C_D \rho_g A_{p,c} \left[\left(u_{g,j} - u_{p,j}\right)\left(u_{g,j} - u_{p,j}\right) \right]^{\frac{1}{2}} (u_{p,2} - u_{g,2})}{2m_p} \quad (3)$$

$$\frac{du_{p,3}}{dt} = \frac{C_D \rho_g A_{p,c} \left[\left(u_{g,j} - u_{p,j}\right)\left(u_{g,j} - u_{p,j}\right) \right]^{\frac{1}{2}} (u_{p,3} - u_{g,3})}{2m_p} - \frac{(\rho_p - \rho_g) g_z}{\rho_p} \quad (4)$$

where $u_{p,1}$ and $u_{p,2}$ are the firebrand' velocity in the x and y direction which is generally

the wind direction. Fire plumes blow the firebrands up in the z direction which is the direction of $u_{p,3}$. $u_{g,j}$ is the ambient wind velocity. m_p is the mass of the particle. ρ_p is the density of the particle. The firebrands are blown upwards and this process provides a mechanism for them to travel farther away in the air. If there is no fire plume, the firebrands may still travel on the wildland surface but the friction loss is much higher, thus they will not travel as far when compared to firebrands in the air. The velocity equations above show the relationship between firebrand properties, atmospheric wind velocity and, gravity.

1.3 Objectives and Research Plan

The transport of firebrands depends on the firebrand interaction between the local ambient wind and the fire plume. The velocity field made up by the fire plume and the ambient wind plays an important role for firebrand transport and leads to the fire spotting phenomenon. Up to now, lots of studies have been done on firebrand transport in different velocity fields. For example, Tarifa et al. [14] has done research on how firebrand transport changes with firebrand properties such as size, shape and density in a small wind tunnel. Firebrand transport through a natural convective and swirling plume has been observed by Lee and Hellman [15] and they discussed firebrand aerodynamic behavior and trajectory under the effect of that turbulent plume. Himoto and Tanaka [16] built a model on urban fire spread and estimated the firebrand travel distance.

These previous studies are mainly about firebrands transport and their travel pattern. Mathematical models are built based on assumptions and wildland fire data. Tohidi [17] has done some wind tunnel experiments at Clemson University and developed a detailed database of firebrands transport. He released hundreds of particles in a controlled

environment corresponding to a wind tunnel and recorded the trajectories of individual particles. Based on the measured flow velocities in the wind tunnel and particle properties, Tohidi also performed numerical simulations of his experiments using OpenFOAM. The OpenFOAM results were found to be in good agreement with the experimental data.

In this study, our objective is to replicate Tohidi's simulations of his previous firebrand transport experiments using FDS [18]. Based on the same wind tunnel velocity field configuration and particle properties, particles have been released in FDS and their flying patterns have been generated to be compared with the experiment data from the wind tunnel experiment. Particular attention is paid to matching the measured velocity field of the vertical jet and cross-wind. The shape, density and size of the particles released in FDS are the same as the particles released in the wind tunnel experiments. Here the model is built up using large eddy simulations (LES) in FDS and the turbulence settings has been selected to guarantee that the simulated jet and cross-flow are turbulent. This FDS study can help improve our understanding of the processes in firebrand transport. It also provides a validation test for the FDS model. This FDS study is an useful application to firebrand transport, and it can also be expanded to all problems with transport of solid particles in a turbulent velocity field.

Chapter 2: Wind Tunnel Experiments

The tests are conducted in a wind tunnel with open boundaries in the stream-wise direction. The wind tunnel in this experiment is 3 m wide, 2.03 m high and 20 m long. The size of the two inlet and outlet boundaries is 3 m wide and 2.03 m high. The streamwise (horizontal) flow comes from inlet boundary while outlet boundary of the wind tunnel remains open to the environment which helps the pressure field being steady. This streamwise flow provides the particles streamwise velocity so they could travel in the horizontal direction of the wind tunnel and it simulated the presence of a surface wind in real wildland fires. A jet flow blows the particles in the upward vertical direction which simulates the action of a fire plume in real wildland fires. The particles are injected near the base of the vertical jet.

2.1 Streamwise Velocity Blower Diagnostics

The streamwise wind blower has a reference velocity of 1.79, 2.23 and 2.85m/s measured at an elevation of z_0 = 0.04 m. The velocity follows a power law, which means that the streamwise velocity increases with elevation:

$$\bar{U} = U_0(\frac{z}{z_0})^{\alpha} \tag{5}$$

To make the streamwise velocity have different values for different velocity fields, the air blower speed dial level has been set as 0.5, 1 and 2 for 1.79m/s, 2.23m/s and 2.85m/s cases. The anemometers have been set at the centerline of the blower, 25 cm upstream of the vertical jet centerline, to collect the horizontal streamwise velocity data from the blower. The vertical jet is inactive when measuring the horizontal velocity profiles. In these three different velocity cases, each case corresponds to a different value of the exponent α.

Table. 1. Different power law exponent α for U_0

U_0 (m/s)	1.79	2.23	2.85
α	0.16031	0.1644	0.18936

In a real wildfire, the presence of turbulence causes velocity fluctuations. This turbulent flow affects how high the firebrands can be blown and where they can land. It is important to simulate the turbulence of the streamwise flow. In the experiment, large spires set at the entrance of the test section and roughness elements on the wind tunnel's floor are used to generate turbulent perturbations in the test section. The Cartesian coordinate system velocities are u, v, w and their averaging fluctuations are urms, vrms, wrms.

$$\emptyset_{rms} = \sqrt{\frac{\sum_{i=1}^{n}(\emptyset_i - \bar{\emptyset})^2}{n-1}} \tag{6}$$

The flow fluctuation are measure by turbulence intensity, which is calculated by:

$$I = \frac{URMS}{U} \tag{7}$$

The streamwise turbulence intensity is around 20% near the wind tunnel floor (at z = 0 m) and drops gradually with elevation. When it reaches the ceiling height (at z = 2 m), the turbulence intensity is around 15% [19].

2.2 Jet Velocity Blower Diagnostics

Besides the streamwise wind blower, there is a jet blower on the wind tunnel floor. This jet blower blew flow upward toward the wind tunnel's ceiling. This vertical jet simulates a fire plume that transports firebrands upwards in real wildland fires. There is still slight difference between having a jet and having a real fire plume, because when the plume raises up, its buoyancy generates additional vertical momentum while the vertical jet has a constant momentum flux. The density of a plume is lower compared to the constant

density of the jet. The effect of these two factors is negligible while considering the trajectory of the firebrands. Therefore, here in the wind experiment, using the vertical jet can provide validated data and avoid the complications of a fire.

The jet has a reference velocity of 8 m/s, 9 m/s and 12 m/s on the centerline at an elevation z = 0.138m above the jet exit. The jet center is on the wind tunnel floor and it is located 1 m downstream of the entrance of the test section. The jet has a circular exit which R = 0.076m. In FDS, the shape of the computational cells are cubic or cuboid, so the circular jet is treated in FDS as a square jet with the same cross-section area. The length of the side of this square is 0.134m.

The air flow of the jet is generated by flexible hoses connected to blowers. The hoses go through a 58.8 cm flow straightener with a honeycomb mesh and then reaches the jet exit. Therefore, the vertical flow coming out from the jet exit is highly turbulent and the jet potential core is eroded approximately three jet diameters downstream of the jet exit nozzle. The measured velocities of the jet are consistent with classical round jets data [20]. It is reasonable to use the integral model here to quantify the vertical jet velocity parameters.

$$\langle U_{(j|r=0)} \rangle = 7{M_0}^{1/2} z^{-1} \tag{8}$$

where M_0 is the initial momentum of the flux just coming out of the jet exit, z is the vertical distance from the surface of the jet exit. In real wildland fires, the flux momentum is related to the buoyancy and the fire heat release rate. Based on the equation above, the vertical velocity decreases with the elevation z on the centerline of the round jet.

2.3 Particle Properties

These wind tunnel experiments use non-combusting polyurethane particles instead of using the burning firebrands. The density of this material is $\rho = 30 kg/m^3$; the side aspect ratio is $\eta_s = \frac{L_x}{L_y} = 1$; and the particles use three different values of the longitudinal aspect ratio $\eta = \frac{L_z}{L_{x,y}} = 1, 4$ and 6. Very little is known in the wildland fires on firebrands size and shape. The firebrands have three different sizes in these wind tunnel experiments. In the case $\eta = 1$, the size of the firebrands is $L_x = L_y = L_z = 1$ cm; and in the other cases, the size of the firebrands is $L_y = L_z = 0.5$ cm. As mentioned before, these firebrands are non-combusting. In this experiment, there is no fire or any other source of heat to make the particles burn. The pyrolysis and charring of firebrands are not considered in these wind tunnel experiments. The particles have been released with no initial orientations. The initial released position was at z = 0.005m above the jet nozzle.

To provide sufficient samples, each aspect ratio particles have been released around 200 times in the given velocity field. There is a total of nine combinations of the atmospheric wind and jet velocity fields. In each of these nine velocity fields, each aspect ratio group of 200 particles have been released which took approximately 480 s, respectively. A GC-PX 100, JVC camera was installed on the side view of the test section to record the trajectory of firebrands with a resolution of 60 frames per second. An image processing algorithm is used to capture the full trajectory of the particles.

2.4 Experimental Results

For the streamwise velocity profiles, the data collected in the wind tunnel experiments should be consistent with the power law presented in Eq. (5). For the three

cases (1.79 m/s, 2.23 m/s and 2.85 m/s), Fig. 1 shows a comparison between the measured and analytical profiles.

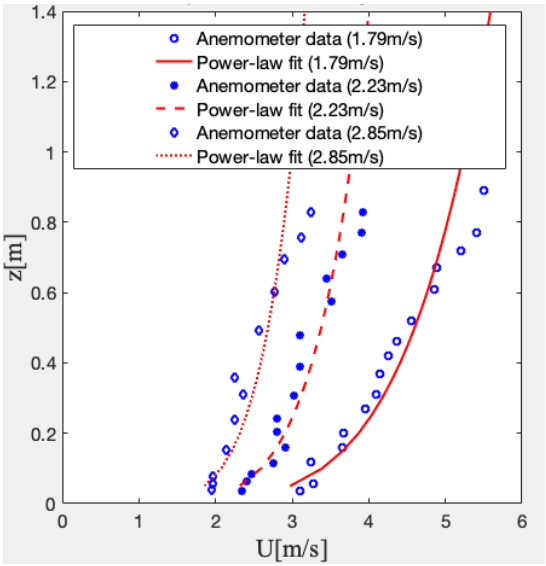

Fig.1. Wind velocity profiles near the inlet of the test section of the wind tunnel (figure taken from [18]).

From right to left, the red solid lines designate the power law for the cases 1.79 m/s, 2.23 m/s and 2.85 m/s, respectively. The blue symbols are the corresponding time-averaged anemometer data. Figure 1 shows that the anemometer data in the wind tunnel experiment are close to the suggested power law.

For the vertical jet, the vertical velocity decays with radial and vertical distance. The vertical velocity is highest near the jet exit and decreases with elevation, it becomes 0 when the jet flow reaches the ceiling of the wind tunnel (see Fig. 2). There is no velocity probe near the ceiling of the wind tunnel so the decay to 0 is not observed in the figure. From left to right in Fig. 2, below are the three centerline velocity profiles for the cases 8 m/s, 9 m/s and 12 m/s, respectively.

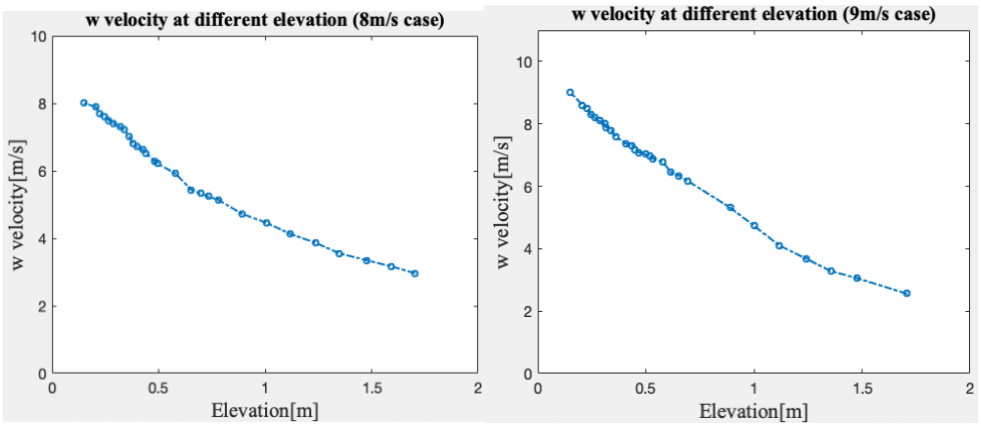

(a) (b)

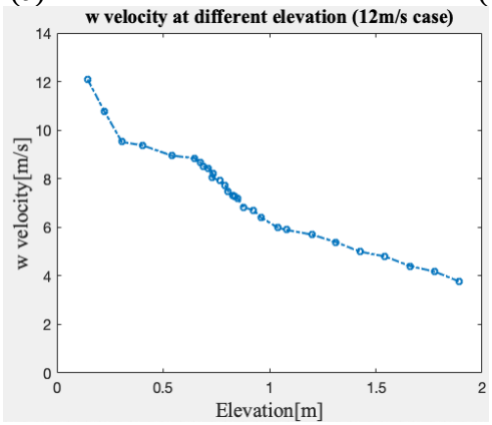

(c)

Fig. 2. Jet centerline velocity profile (figure taken from [18]). (a), (b) and (c) are for cases 8 m/s, 9 m/s and 12 m/s, respectively.

Figure 3 presents the corresponding radial velocity profiles measured at an elevation of z = 0.138m from the jet exit. As it talked above, the velocity has the highest value at the jet center and then it starts dropping and decreases to 0 at the edge of the jet.

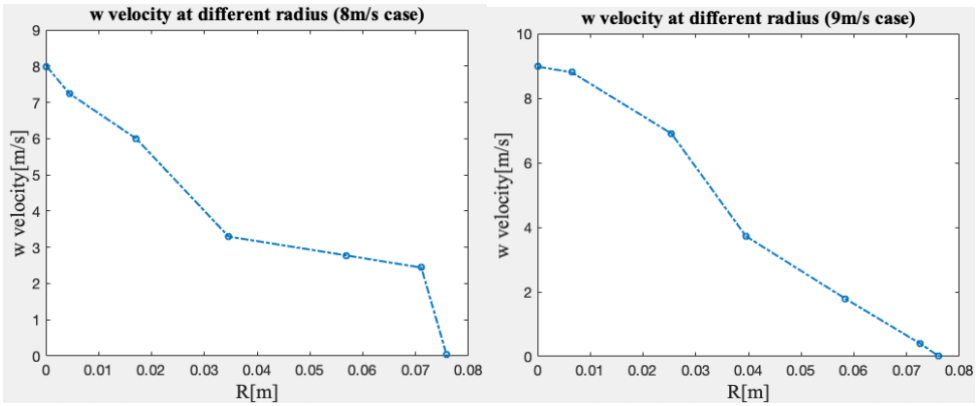

(a) (b)

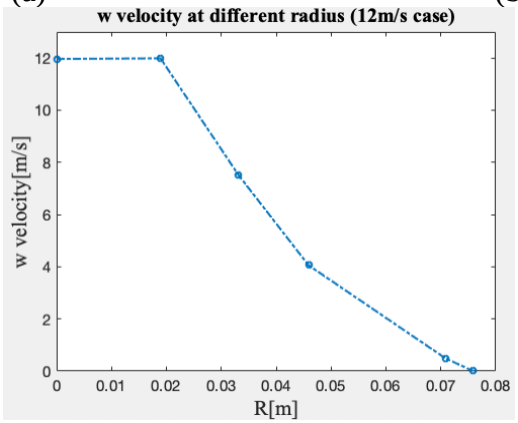

(c)

Fig. 3. Jet radial velocity profile (figure taken from [18]). (a), (b) and (c) are for cases 8 m/s, 9 m/s and 12 m/s, respectively.

In the experiments with particles, the velocity field is a combination of the wind tunnel horizontal velocity and the vertical jet velocity. The particles have been released near the base of the jet and move in the vertical and horizontal directions. The trajectory of particles is close to a parabola. Figure 4 present representative trajectories obtained for the $\eta = 1$ particles with $U_0 = 2.85\ m/s$, $U_{(j|r=0)} = 12\ m/s$.

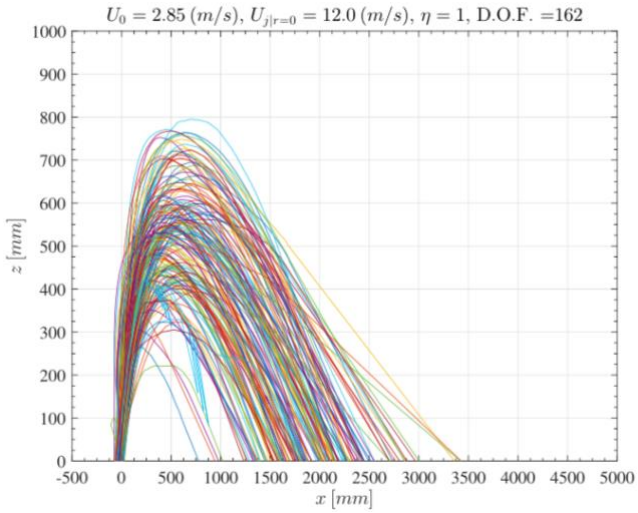

Fig. 4. Trajectories of particles (figure taken from [18]).

The particles downwind distance x_l and maximum lofted height z_{max} have been recorded and analyzed for each of the nine different velocity fields and for different values of the particle aspect ratio. The probability density functions (PDFs) of normalized downwind distance, $\frac{x_l}{z_m}$, where x_l is the maximum downwind distance and z_m is the height at which the jet flow becomes significantly bent over by the cross-flow, the PDFs of normalized maximum rise height, $\frac{z_{max}}{z_m}$, z_{max} is the maximum rise height, and the PDFs of normalized downwind distance with maximum lofted height, $\frac{x_l}{z_{max}}$, are calculated based on the trajectory data for different cases and compared to the numerical simulation data.

Chapter 3: FDS Configuration

3.1 FDS Domain and Grid Settings

The FDS configuration is based on the wind tunnel experiment setup. The computational domain corresponds to a portion of the wind tunnel test section. The wind tunnel test section is 3 m wide, 2.03 m high and 20 m long. It is located between $x = -1$ m to 19 m, $y = -1.5$ m to 1.5 m and $z = 0$ m to 2.03 m for the wind tunnel experiments. Because the farthest downwind transport distance of the particles is around 3.5 m in the experiments, the FDS computational domain is set as 5 m to be long enough to let the particles land. The size of the whole wind tunnel domain in FDS is approximately 3 m wide, 2 m high and 5 m long. The computational domain is located from $x = -1.0452$ m to $x = 3.9932$ m, from $y = -1.5008$ m to $y = 1.5008$ m, and from z = 0 m to z = 2 m.

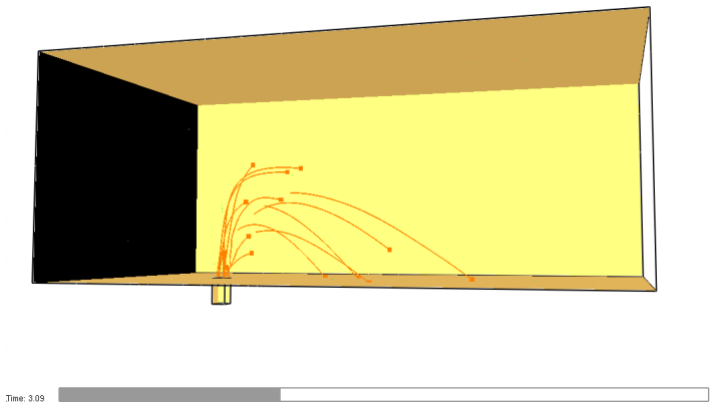

Fig. 5. FDS domain

When it comes to simulating the experiments in FDS, the spatial solution is an important factor to be considered. Large grid cell sizes can save simulation time but cannot capture the details of the flow inside the computational domain so the accuracy is negatively impacted. Small grid cell sizes require more computational resources but the accuracy is increased because the computational grid can capture the details of the flow

inside the simulation domain. Whether the grid is large or small depends on the characteristic sizes of the dominant turbulent flow features present in the problem under consideration. The size of the grid should capture these dominant features well. Generally, the grid cell size should be selected as smaller than $1/10_{th}$ or $1/20_{th}$ of the characteristic length scales of the problem. The basic grid cell in FDS is rectangular-shaped, it cannot be a cylinder or a sphere. For example, to simulate the round jet that provides vertical momentum in the wind tunnel experiments, the shape of the round jet has to be modified and treated as a square in FDS, with the same cross-section area. The side length of the square is 0.134 m and this length scale needs to be captured by the grid: thus, the grid cell size in the region of the vertical jet will be on the order of $1/10_{th}$ of 0.134 m, or 0.0134 m.

While the grid cell size is around 0.0134 m in the jet region, because of limited computational resources, this cell size is too small to be applied to the whole computational domain. Note that abrupt changes in the grid cell size can cause numerical instability and decrease the accuracy of the simulations. In the design of the computational grid, we use different blocks with changes of grid resolution between adjacent blocks by a factor 2. The grid resolution is $0.0134\ \text{m} \times 0.0134\ \text{m} \times 0.01\ \text{m}$ in the jet near-field region and decreases to $0.0268\ \text{m} \times 0.0268\ \text{m} \times 0.02\ \text{m}$ in the jet far-field region. The resolution further decreases by additional factors of 2 to $0.0536\ \text{m} \times 0.0536\ \text{m} \times 0.04\ \text{m}$, and to $0.1072\ \text{m} \times 0.1072\ \text{m} \times 0.08\ \text{m}$ in the bulk of the simulated test section of the wind tunnel. The mesh setting in the FDS simulation is shown as below.

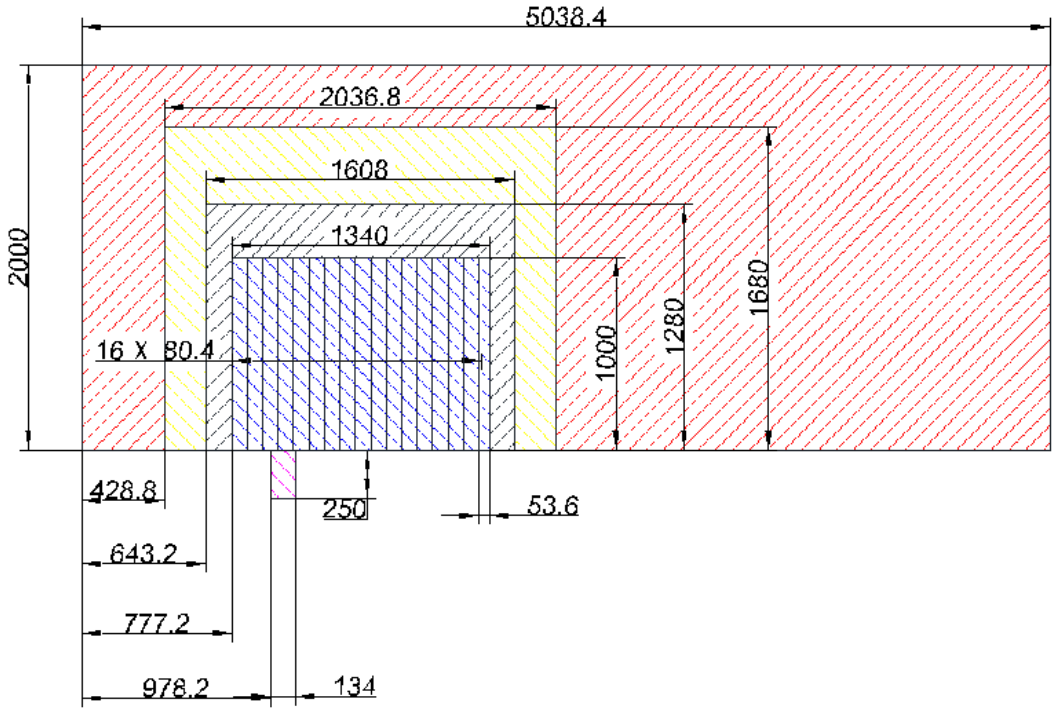

Fig. 6. FDS mesh setting (dimension in milimeters)

3.2 Velocity Field and Particles in FDS

In FDS, the streamwise wind blower is set at the inlet boundary of the computational domain. It is located at the plane $x = -1.0452$ m. The area of this blower is 3 m × 2 m. In the experiments, three cases with different streamwise velocities were studied: the mean streamwise velocity is 1.79 m/s, 2.23 m/s or 2.85 m/s at $z_0 = 0.04$ m. The imposed numerical flow in FDS is set to follow a prescribed power law (equation (5)) by using the 'PROFILE' functionality and selecting the setting 'ATMOSPHERIC' [21]. The 3 different velocity cases have different power law α values: 0.16031, 0.1644 and 0.1894. A turbulent inflow boundary condition is used in FDS to simulate the turbulence of the incoming wind flow. The eddy number (N_EDDY) is set as 100. The characteristic eddy length scale (L_EDDY) is set as 0.7. The root mean square (RMS) velocity fluctuation (VEL_RMS) is set as 0.4, 0.5 and 0.65 for 1.79 m/s, 2.23 m/s and 2.85 m/s streamwise velocities, respectively. These choices make sure that the turbulence intensity

is around 20% near the floor of the wind tunnel. They are determined by trial and error through comparisons with the experimental velocity data.

In the wind tunnel experiments, the vertical jet flow is generated by flexible hoses connected to blowers. Those hoses go through a straightener and connected to the wind tunnel floor. In FDS, the vertical jet blower is located at the bottom end of a 0.25 m long duct section that connects to the floor of the wind tunnel. The square duct is located between $x = -0.067$ m and $x = 0.067$ m, $y = -0.067$ m and $y = 0.067$ m, $z = -0.25$ m and 0 m and it is open to the wind tunnel at the z = 0 m surface. The streamwise wind blower is located at the plane $x = -1.0452$ m, so the center of the jet is approximately 1 m downstream of the inlet of the computational domain. In the experiments, three cases with different jet velocities were studied: the jet injection velocity is 8 m/s, 9 m/s or 12 m/s, at z = 0.138m on the centerline of the jet. Experimental velocity profiles suggest that the turbulent jets have a short potential core and undergo rapid mixing, which suggest the presence of strong jet turbulence. A turbulent inflow boundary condition is used in FDS to simulate the turbulence of the incoming jet flow. The eddy number (N_EDDY) is set at 100. The characteristic eddy length scale (L_EDDY) is set at 0.067, which is half of the side length of the duct. The root mean square (RMS) velocity fluctuation (VEL_RMS) is set at 2 for 8 m/s, 9 m/s and 12 m/s spanwise velocities. These choices are determined by trial and error through comparisons with the experimental velocity data.

The particles are released right above the jet surface (at z=0.005 m) around t = 2 s when the velocity field is fully developed in FDS. The particles are released every 0.01 s without initial velocity. The particles in FDS are made of the same material used in the experiments. They are made of polyurethane, which has a density of 30 kg/m^3. The particles in the FDS simulation are treated as chemically inert particles. These particles are

rectangular-shaped and have 3 different sizes, $\eta = 1, 4$ and 6. η is the longitudinal aspect ratio, $\eta = \frac{L_z}{L_{x,y}}$. L_x, L_y and L_z is the particle length in the x, y and z directions. In the case $\eta = 1$, the size of the firebrands is $L_x = L_y = L_z = 1$ cm. For $\eta = 4$ case, the size of the firebrands is $L_y = L_z = 0.5$ cm and $L_x = 2$ cm. For $\eta = 6$ case, $L_x = 3$ cm and $L_y = L_z = 0.5$ cm. The number of the particles is around 500 for every different η.

3.3 FDS Velocity Field Results

To measure the streamwise velocity coming out of the wind blower, the FDS velocity sensors have been set at the same location as that used in the experiments, on the centerline of the test section and 0.25 m upstream of the vertical jet centerline. The velocity sensors are set every 0.1 m from z = 0.05 m to 1.95 m. These velocity sensors measure the mean and RMS vertical profiles of streamwise velocity; the vertical jet is turned off in these simulations. The FDS results are compared with experiment anemometer data and the power law fit.

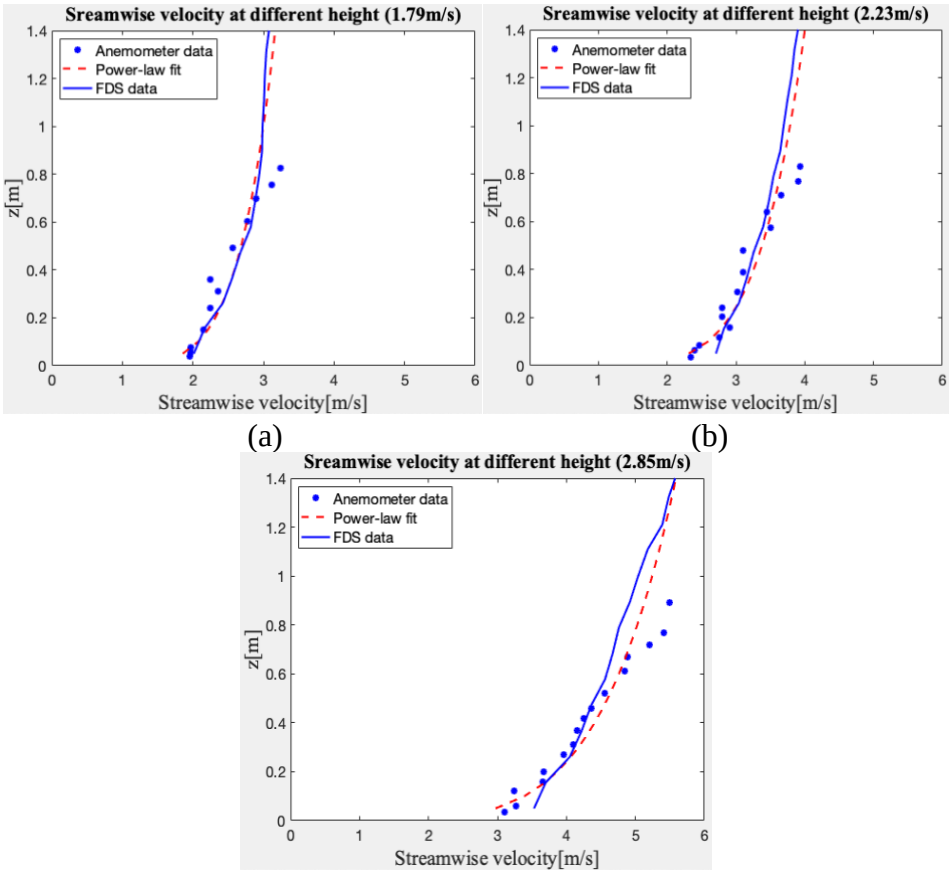

Fig. 7. Comparisons between the simulated and measured streamwise velocity near the entrance of the wind tunnel test section (experimental data taken from [18]). (a), (b) and (c) are for cases 1.79 m/s, 2.23 m/s and 2.85 m/s, respectively.

Figure 7 shows that the streamwise velocity increases with elevation in the wind tunnel. This increase is significant. The experimental data (blue symbols) also suggest that the thickness of the boundary layer on the floor of the wind tunnel is very thin. This boundary layer is not resolved in the FDS simulations. Figure 7 also shows that the power law used to impose the mean inflow velocity profile (Eq. (5)) provides an approximate but fair approximation of the variations of streamwise velocity with elevation.

Figure 8 presents similar results in terms of turbulence intensities, defined as the RMS value of streamwise velocity divided by the mean streamwise velocity.

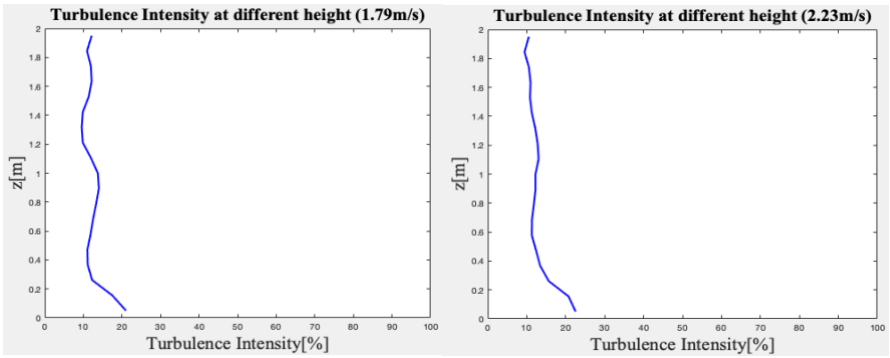

(a) (b)

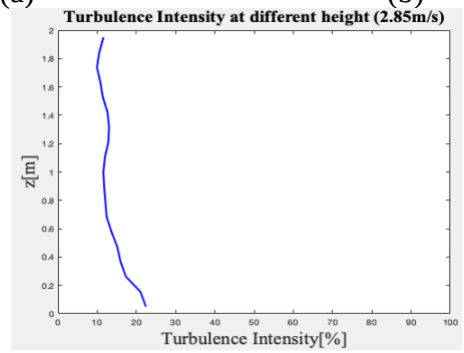

(c)

Fig. 8. Simulated turbulence intensity for the streamwise component of velocity near the entrance of the wind tunnel test section. (a), (b) and (c) are for cases 1.79 m/s, 2.23 m/s and 2.85 m/s, respectively.

In all of these 3 cases, the turbulence intensity is slightly higher near the wind tunnel floor and decreases with elevation. This is because the setting 'VEL_RMS' defines the velocity fluctuation at z = 0.04 m and as shown in Fig. 7, the mean streamwise velocity increases with elevation so at higher elevations, the value VEL_RMS is divided by a larger mean streamwise velocity, which explains the decrease in turbulence intensity with elevation. The intensity is around 20% near the wind tunnel floor and drops to 10% near the ceiling.

To measure the vertical velocity coming out of the jet blower, the FDS velocity sensors have been set at the same location as that used in the experiments. The velocity sensors have been set on the centerline of the jet blower from $z = -0.25$ m to z = 2 m. From $z = -0.25$ m to z = 1 m, the velocity sensors have been placed every 0.01 m because

the grid size is small in that region and around 0.01 m resolution. From z = 1 m to z = 1.5 m, the velocity sensors have been placed every 0.05 m because the grid size is larger in that region. From z = 1.5 m to z = 2 m, the velocity sensors have been placed every 0.1 m because the grid size is even larger in that region and around 0.1 m resolution. These velocity sensors measure the mean and RMS vertical profiles of vertical velocity; the horizontal wind is turned off in these simulations.

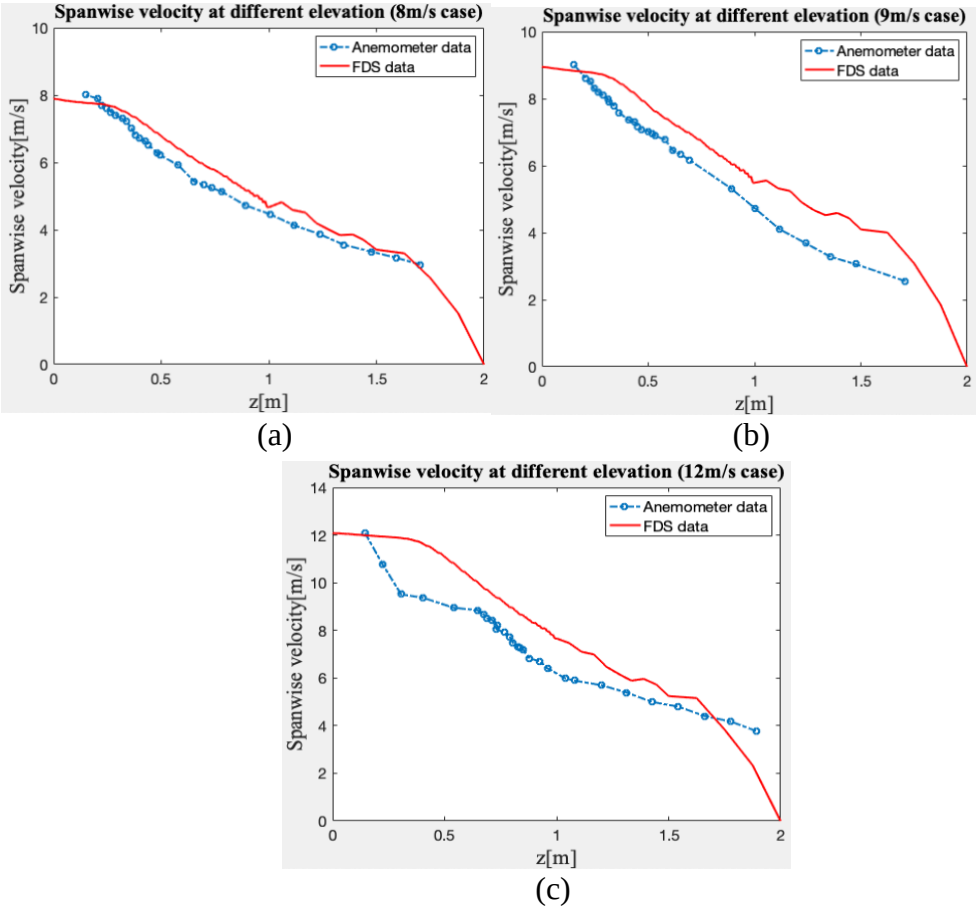

Fig. 9. Comparisons between the simulated and measured vertical velocity along the centerline of the vertical jet (experimental data taken from [18]). (a), (b) and (c) are for cases 8 m/s, 9 m/s and 12 m/s, respectively.

In Fig. 9, the blue lines with symbols are the experiment data, and the solid red lines are the FDS results. Because in the experiments, there is no velocity probe near the ceiling of the wind tunnel, the stagnation region and the decay to 0 velocity is not observed in the

experimental data. Note that in the experiments, there is no velocity probe near the floor of the wind tunnel so the near-field velocity dynamics are not characterized either. Figure 9 shows the expected decay of centerline jet velocity with elevation due to mixing. It is not clear whether the jet has a well-defined potential core. The FDS results are not smooth from z = 1 m to z = 2m. This is because the mesh becomes coarser beyond z = 1 m.

Figure 10 presents similar results in terms of radial profiles of vertical velocity at the elevation z = 0.14 m. The velocity sensors have also been placed at intervals of 0.0134 m from the center to the edge of the jet. It seen that the while simulations indicate the presence of a potential core in all jet velocity cases, the experimental data suggest that there is no potential core and that the velocity rapidly decays from peak value on the jet centerline when moving in the radial direction. The experimental velocity profiles do not correspond to a canonical turbulent jet structure, which suggest that the experimental jets are strongly perturbed by the supply system.

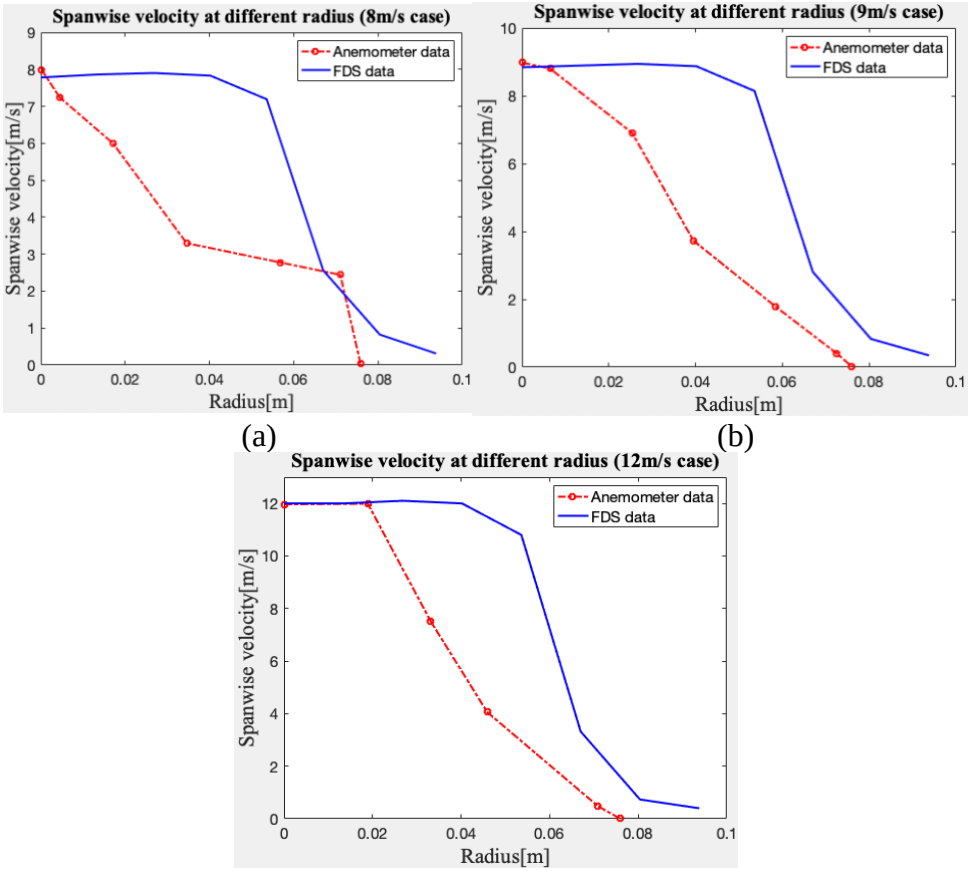

Fig. 10. Comparisons between the simulated and measured vertical velocity versus radial distance at an elevation z = 0.14 m (experimental data taken from [18]). (a), (b) and (c) are for cases 8 m/s, 9 m/s and 12 m/s, respectively.

Figure 10 shows the expected decay of vertical jet velocity with radial distance due to mixing. The FDS simulations predict that at z = 0.14 m, the jet has a well-defined potential core (a region of uniform velocity and low turbulence levels). The experimental data do not feature a well-defined potential core. These results suggest that the experimental jet does not feature a canonical turbulent jet structure. They also reveal a significant level of discrepancy, particularly in the near-field region of the jet, between the simulations and the experiments.

Chapter 4: FDS Result and Comparisons to Experimental Data

4.1 Post-processing of Particle Trajectories in the Experiments and Simulations

Camera were used in the wind tunnel experiments to record the particle trajectories. The camera videos were analyzed using an image processing algorithm that starts with extracting all frames in a video and constructing a background image. Using MATLAB, the images are read and converted. The background image is constructed by averaging over light intensities of at least 100 empty images and is then subtracted from all frames. Yet, the obtained images are not directly useful to get the particle trajectories. This is because the particles rotate while they get lofted and travel downwind. Rotation causes the particles to emit various range of light intensities and it makes it hard to identify them from the background frames. To solve this problem, a rotationally symmetric low-pass Gaussian filter has been used with the background subtracted frames [18]. It helps to distinguish the particles from the background frames because now they have different light intensities. By analyzing the light intensities in the images, the particle trajectories can be obtained.

For FDS simulation, the size of the simulation domain here is $5\ m\ \times\ 3\ m\ \times\ 2\ m$. It has been divided into 33 meshes and 33 processors have been assigned for each mesh. For the mesh which has the most grids, there are 24,000 grids in that mesh. The whole simulation took around 30 h to run for 10 s in simulation. For the result, there are over 1000 particle trajectories that are simulated. Therefore, the simulation is pretty effective and computational resources needed for this simulation is acceptable. The simulation time (30 h) is also in a reasonable time range by using the multiple meshes setting.

The whole simulation process can be viewed in Smokeview. Smoeview is the graphics display package released with FDS. The Smokeview videos show the particles from their release near the jet exit, travel within the wind tunnel and up to their landing at some downstream distance. The particles trajectories are shaped like a parabola. The particles move mainly in the x and z directions, because the streamwise flow and vertical flow blow in these two directions. The trajectories are three-dimensional, however, with some lateral spread, but only a small lateral spread is observed in the experiments as well as in the simulations. Most particles are clustered around the centerline of the tunnel directly downwind of the release location. It is important to know how high and how far the embers can travel in actual WUI fires, so in the experiments and simulations, it is important to analyze the particle maximum elevation, z_{max}, and the particle maximum downwind distance, x_l. The observed lateral spread is small relative to z_{max} and x_l. To collect data on z_{max} and x_l, it is necessary to convert the Smokeview particle file into a plot of the particle trajectories in the x-z plane. Below is a screenshot of Smokeview showing simulated particles trajectories in the wind tunnel.

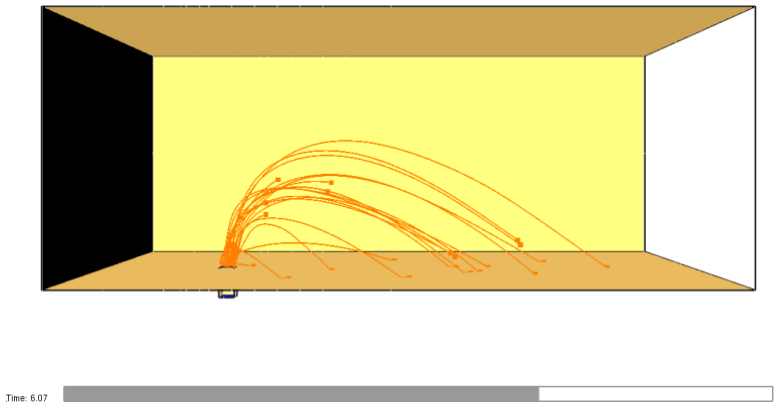

Fig. 11 Smokeview representation of simulated trajectories of reference particles ($\eta = 1$) under a given velocity field ($U_0 = 2.85\ m/s$, $U_{(j|r\,=\,0)} = 12\ m/s$)

FDS does not have a function to save trajectories of individual particles directly. Data related to particles are saved into .prt5 files that are organized by mesh. In the present work, the test section of the wind tunnel has been divided into multiple meshes (Fig. 6), and every mesh has it own .prt5 file recording how the particles travel inside that particular mesh. To reconstruct the whole particle trajectory, the data from different .prt5 files need to be read and combined together. FDS is a FORTRAN program, when data are saved in .prt5 files, particles are labeled using FORTRAN language. In the output .prt5 files, the particle label and its trajectory data are both recorded. This makes it possible to combine the particle trajectory data from multiple meshes, because the label of the particle can serve as a clue to find the parts of the trajectory of that specific particle distributed over different meshes. The .prt5 files are read and then combined using an in-house MATLAB post-processing program.

4.2 Comparisons of Measured and Simulated Particle Trajectories

Because there are total 27 cases, one of those cases has been selected as an example to show what the particle trajectories plot looks like. Below is the simulation particle trajectories plot corresponding to $U_0 = 2.85\ m/s$, $U_{(j|r\,=\,0)} = 12\ m/s$ and the particle aspect ratios $\eta = 4$.

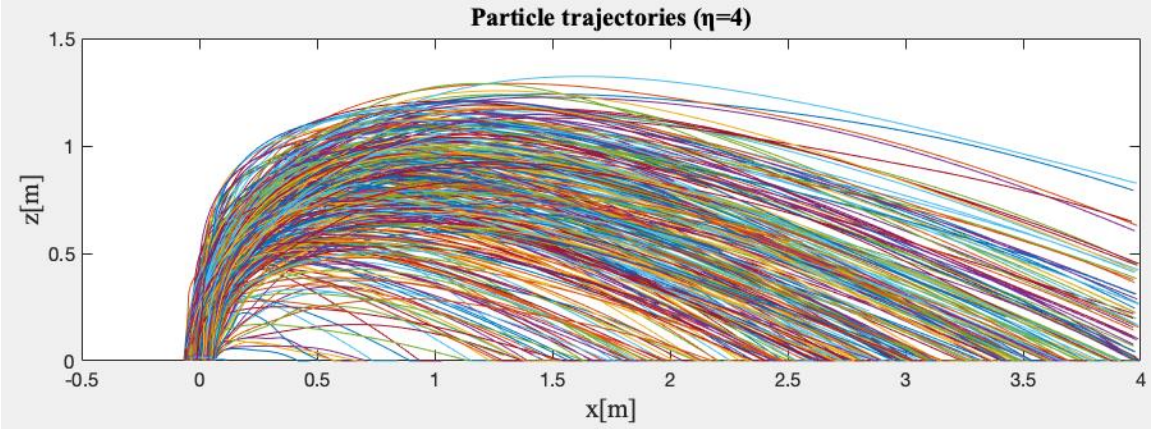

Fig. 12. Trajectories of particles in FDS simulation corresponding to $U_0 = 2.85\ m/s$, $U_{(j|r=0)} = 12\ m/s$ and particle longitudinal aspect ratio η=4.

The number of released particles in each case is around 500. It can be seen in Fig. 12, the particles have been lofted, blown in the downwind direction before landing further downwind. Some of the particles have flown out of the domain, but most of the particles land on the floor before leaving the computational domain. Below is the comparison of the simulation particle trajectories and the experimental particle trajectories.

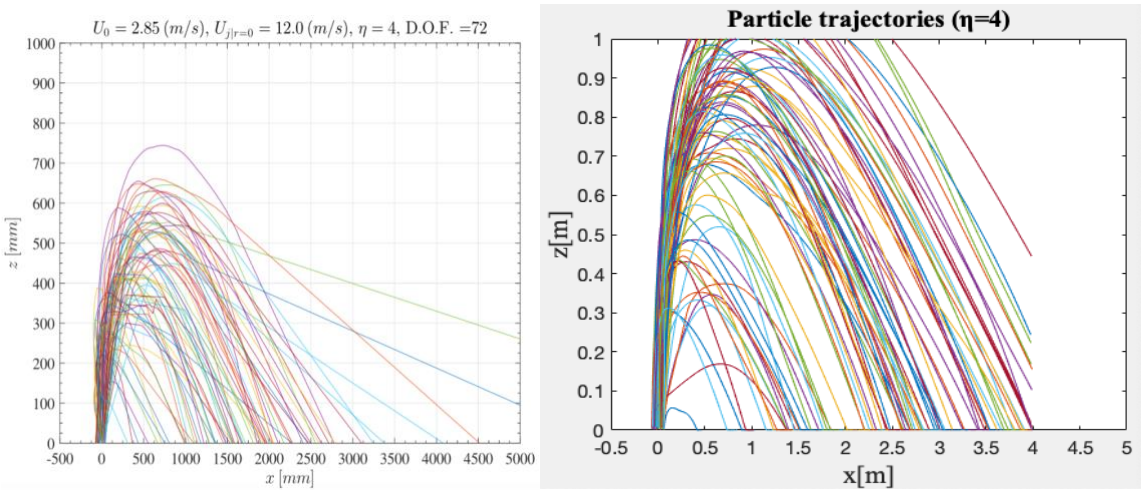

(a) (b)

Fig. 13. Trajectories of particles corresponding to $U_0 = 2.85$ m/s, $U_{(j|r=0)} = 12$ m/s and particle longitudinal aspect ratio η=4. (a) is the plot of 72 particles trajectories in the experiment. (b) is the plot of similar number particles trajectories in the simulation. (experimental data taken from [18])

In Fig. 13 (a), the D.O.F. number is the number of particles that has been recorded. This number varies between experiments. The variation is due to either the particles leaving the frame of analysis or to low intensity levels of light during the flight that would prevent the camera from correctly recording the trajectory. Despite these problems, most of the trajectories of the particles have been successfully recorded and included in the plots. For Fig. 13 (b), a similar number of particles trajectories are plotted out under the same coordinate system. The trajectories are cut off at x=4 m, this is because the FDS domain has its boundary set at x=4 m. The particles in the simulation has a higher maximum rise height and a farther downwind travel distance, this is probably because the vertical jet in FDS has a potential core, and for where the particles get released, the vertical flow velocity stays as high as center point velocity until it comes to the edge of the jet.

4.3 Particle Trajectory Results

The particle trajectories plots are in agreement with expectations. The particles

which are released near the center of the jet have a higher vertical velocity and it provides them more time to travel before they land on the floor, which explains that the particles released near the jet center have a larger downwind travel distance. Similarly, the particles released near the edge of the jet have a lower vertical velocity and therefore a shorter downwind travel distance. This explains the large variations in the values of the maximum elevation, z_{max}, and downwind distance, x_l.

To compare the measured and simulated particle trajectories, we consider the ratio of downwind distance divided by the maximum elevation, (x_l/z_{max}), and calculate the probability density function (PDF) of this ratio. Also following Tohidi [18], we normalize both x_l and z_{max} by the elevation z_m, defined as the height at which the jet becomes significantly bent by by the cross-flow. For the velocity field $U_0 = 2.85\, m/s$, $U_{(j|r=0)} = 12\, m/s$, z_m is around 0.6 m in both the wind tunnel experiments and FDS simulations. Figure 14 shows the variations of streamwise velocity on the central vertical plane in the FDS simulation. It gives a visual representation of the value of z_m for this case.

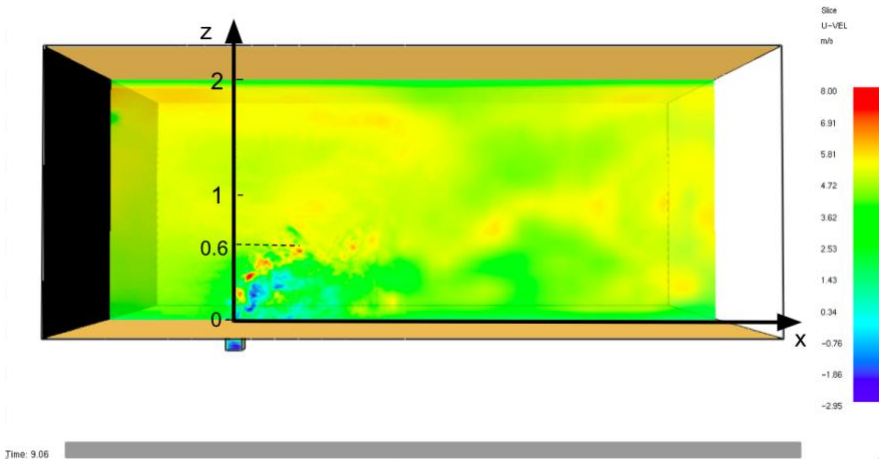

Fig. 14. Streamwise velocity slice in Smokeview corresponding to $U_0 = 2.85\, m/s$, $U_{(j|r=0)} = 12\, m/s$.

Figure 14 shows the bending of the vertical jet flow by the horizontal cross-wind. The elevation where the flow transitions from vertical to horizontal is around 0.6 m.

The experiments have a sample size of 200 particles. Because of the tracking technique, the number of particles for which the full trajectory is successfully observed is around 70-160 with variations between cases. To analyze the statistics of the particle trajectories, a kernel density estimation technique has been adopted [18]. The kernel distribution provides a smooth reconstruction of the probability density function (PDF) of a random variable in the case of small sample size. For any random variable x, the kernel density estimator's formula is given by:

$$\widehat{f_h}(x) = \frac{1}{nh}\sum_{i=1}^{n} K\left(\frac{x-x_i}{h}\right) \tag{9}$$

where x_i is the random variable from an unknown distribution, n is the sample size, K is the kernel smoothing function ($K(u) = \frac{3}{4}(1-u^2)$) and h is the bandwidth, which is a smoothing parameter. The probability density for different x values is a histogram at the

beginning and then it gets smoothed and becomes a smooth curve. The bandwidth h in equation (9) is chosen depending on the sample number n to smooth the histogram into a curve. Thus, the kernel density estimation technique starts with a rough histogram and generates a smooth PDF.

MATLAB has a default function for calculate the kernel density estimator, and a PDF function 'pdf (kernel density estimator, x_l/z_{max})' that is used here to provide the kernel distribution of the ratio of downwind distance divided by maximum elevation (x_l/z_{max}) for different particle aspect ratios. There are 3 different streamwise velocities (8 m/s, 9m/s and 12 m/s) and 3 different spanwise velocities (1.79 m/s 2.23 m/s and 2.85 m/s at $z_0 = 0.04m$). By combining different streamwise velocities with different spanwise velocity, there are 9 different velocity field in total. Figure 15 presents the kernel PDFs obtained in the experiments [18] for 9 different velocity fields.

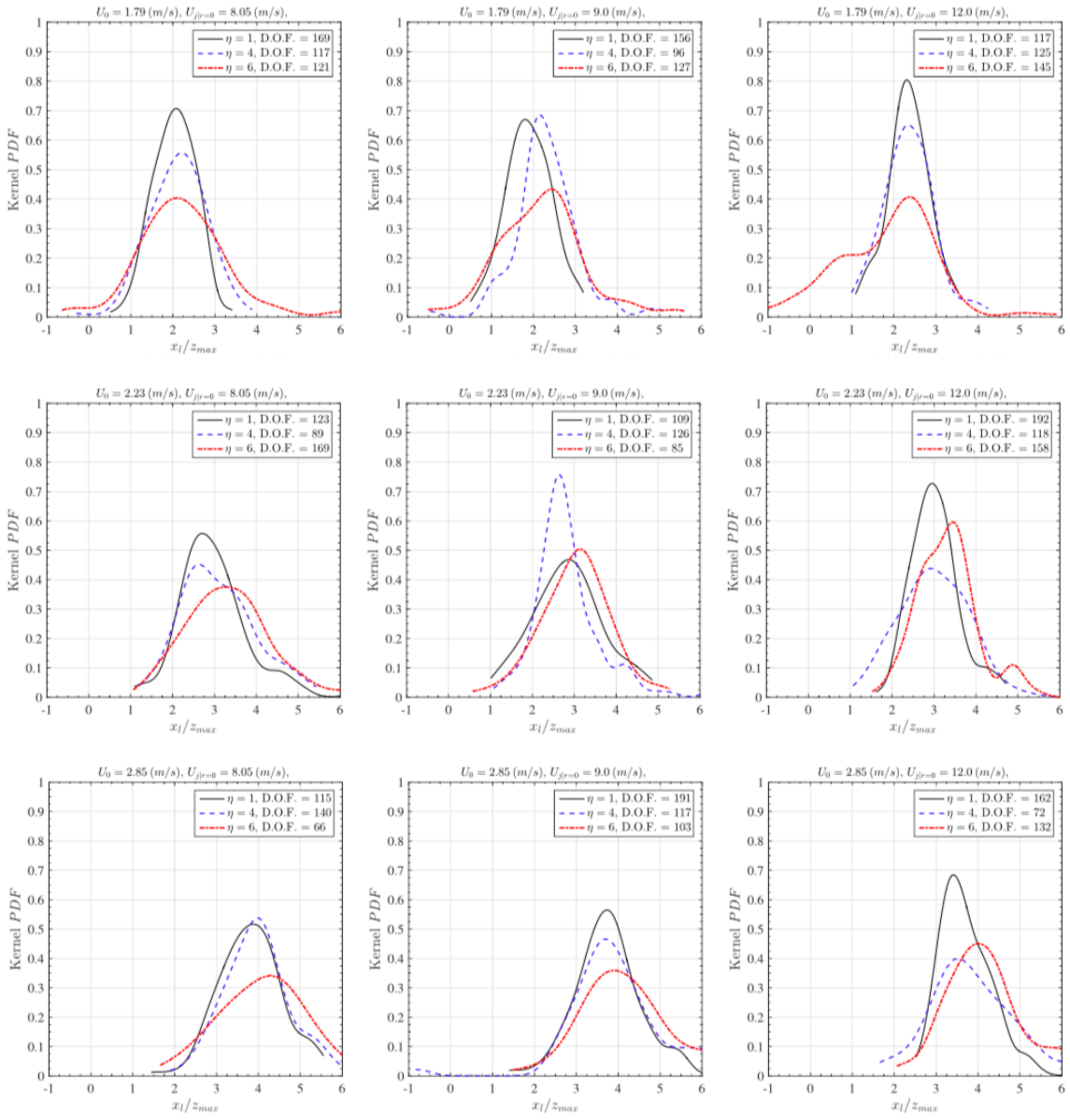

Fig. 15. Experimental estimates of the kernel probability density functions (PDFs) of the ratio (x_l/z_{max}). From left to right, U_0 is constant while $U_{(j|r=0)}$ is increasing. From top to bottom, U_0 is increasing while $U_{(j|r=0)}$ is constant. (experimental data taken from [18])

Figure 15 suggests that the statistical distribution of (x_l/z_{max}) is not significantly sensitive to the value of the particle aspect ratio. The distribution of (x_l/z_{max}) varies with different velocity fields.

In the post-processing of the FDS simulations, the PDFs are calculated using

MATLAB but without the kernel density estimator. This is because the FDS simulations have a bigger sample size for calculating PDFs which is around 280-320. The number of numerical particles released is larger than that used in the experiments. In Fig. 16 presented below, the black solid line corresponding to $\eta = 1$. The blue dashed line corresponding to $\eta = 4$. The red dashed line corresponding to $\eta = 6$.

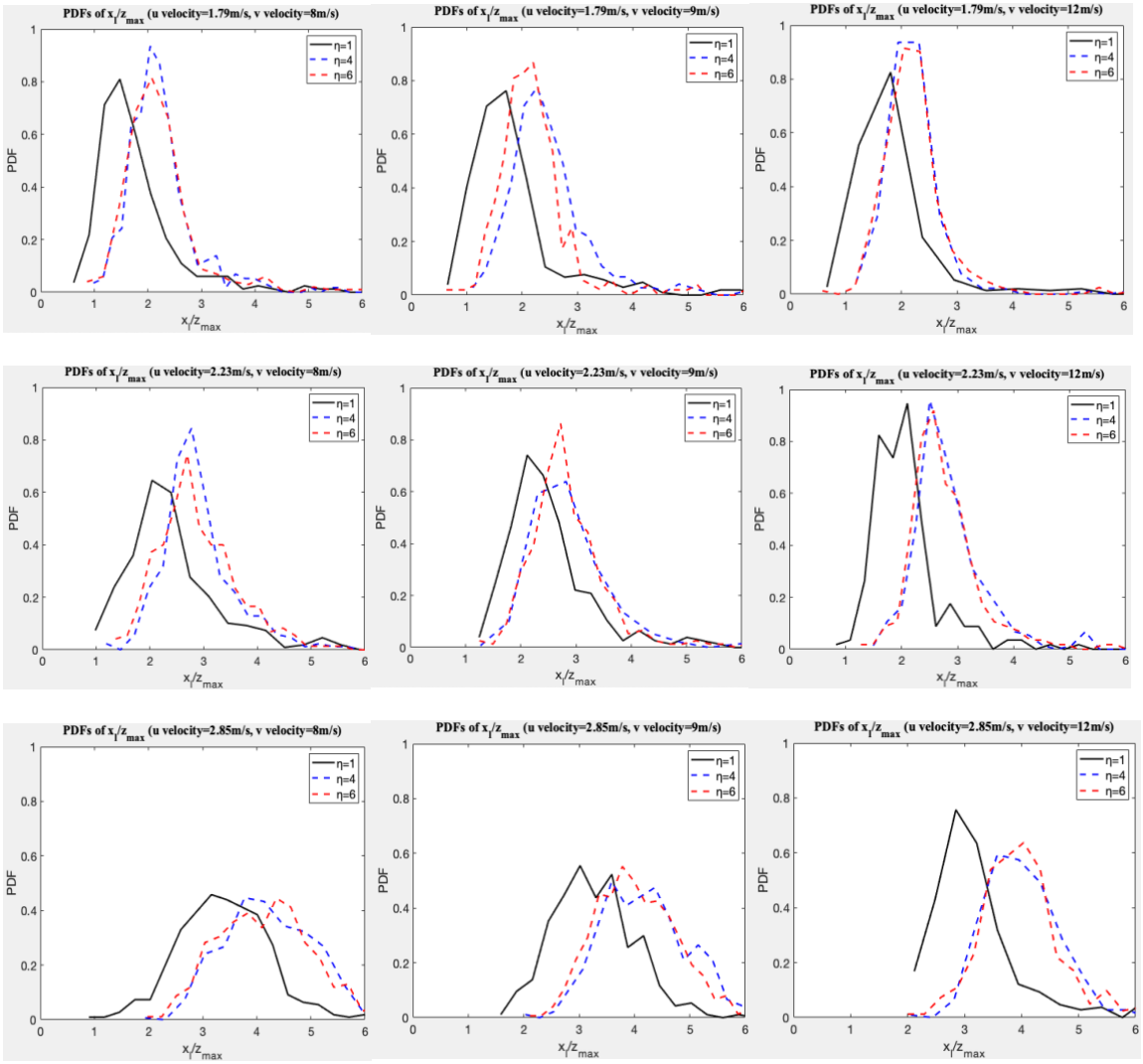

Fig. 16. FDS estimates of the probability density functions (PDFs) of the ratio (x_l/z_{max}). From left to right, U_0 is constant while $U_{(j|r\,=\,0)}$ is increasing. From top to bottom, U_0 is increasing while $U_{(j|r\,=\,0)}$ is constant.

Figure 16 suggests that the statistical distribution of (x_l/z_{max}) is sensitive to the

value of the particle aspect ratio with $\eta = 1$ leading to smaller values of (x_l/z_{max}). Furthermore, the most probable value of (x_l/z_{max}) is increasing with U_0. In the cases $\eta = 4$ and $\eta = 6$, the most probable value of (x_l/z_{max}) has a larger value. There are some particles having larger (x_l/z_{max}) ratios over 6, but there are just 1 or 2 those kind of particles, so the probability density is almost 0 when (x_l/z_{max}) is over 6. Thus the simulated PDFs are somewhat different from the measured PDFs. This may be explained by the fact that FDS does not consider the lift force and possible rotation of particles when it calculates their transport, and it calculated the wind drag force by having the factors of particle surface to volume ratio and particle shape factor which are different here for different longitudinal aspect radio particles (Equation(1)).

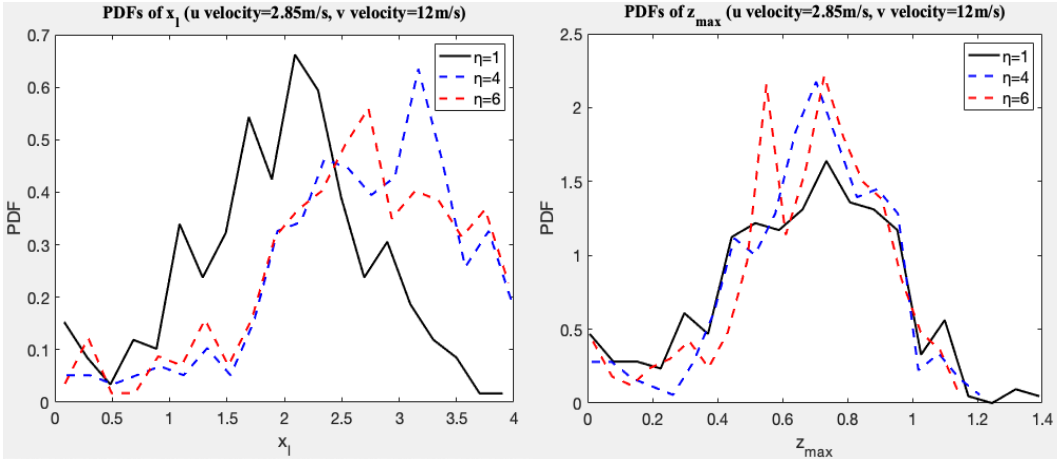

(a) (b)

Fig. 17. (a) is the PDF of downwind disance corresponding to $U_0 = 2.85\text{m/s}$, $U_{(j|r\,=\,0)} = 12\ \text{m/s}$. (b) is the PDF of maximum rise height corresponding to $U_0 = 2.85\ \text{m/s}$, $U_{(j|r\,=\,0)} = 12\ \text{m/s}$.

Fig. 17 shows the particles PDFs of downwind distance and maximum rise height corresponding to $U_0 = 2.85\text{m/s}$, $U_{(j|r\,=\,0)} = 12\ \text{m/s}$. In Fig 17. (a), the statistical distribution of x_l is sensitive to the value of the particle aspect ratio with $\eta = 1$ leading to

smaller values of x_l. Furthermore, the most probable value of x_l is around 1-3 for $\eta = 1$ particles, while the most probable value of x_l is around 2-4 for $\eta = 4$ and 6 particles. From Fig 17. (b), the statistical distribution of z_{max} is not significantly sensitive to the value of the particle aspect ratio. The most particles have a maximum rise height around 0.5-0.9 m.

Chapter 5: Conclusion

Numerical simulations of the transport of particles of different sizes and aspect ratios and subjected to different horizontal and vertical flow are performed with FDS and compared to experimental data. The experimental and numerical data provide insight into the controlling parameters for the transport of firebrands in wildland fire scenarios. In the experiments, the particle trajectories are captured by an image processing algorithm. In the FDS simulations, the output particle files (the .prt5 files) are read using a MATLAB post-processing program and combined to reconstruct and plot the particle trajectories. From the post-processed trajectories, the maximum elevation and downwind distance of the particles are obtained and analyzed. For a given velocity field, the normalized variable is defined as the ratio of landing location divided by maximum elevation, x_l/z_{max}. By plotting the PDFs of (x_l/z_{max}) for different values of the particles aspect ratio, the result show that they have similar probability density functions (PDFs) compared to the experiments. The simulated PDFs are more sensitive to the value of the particle's aspect ratio than the experimental PDFs. This may be explained by the fact that FDS does not consider the lift force and possible rotation of particles.

The present results are focused on how particles travel in a small-scale wind tunnel. The results are thought to be representative of the dynamics of particles in full-scale wildland fires. Note that in the present study, the particles are released without having any initial velocity. They get their momentum from the wind drag forces and gravity. This process is very similar to what happens to firebrands in real wildland fires. The firebrands do not have initial velocity when they break off from the vegetation and the local winds provide the momentum that control their motion.

The research in this paper explores the simulation and post-processing capabilities in FDS towards the study of firebrand transport. In the present work, particular attention was paid in the setting of velocity boundary conditions in order to represent the horizontal wind and vertical jet flows. The jet simulates the presence of a fire plume. The simulated horizontal wind and vertical jet flows are set to be turbulent flow. It is found that the experimental jet does not have a canonical turbulent structure and that the near-field behavior cannot be represented accurately in FDS. In FDS, the simulated particles are released at prescribed time intervals. Because the particles are automatically labeled in the FDS output files, there is no need to have a long time interval between particle release. This can shorten the simulation time significantly. The post-processing algorithm can combine the information on particle trajectories distributed on different meshes and plot out the whole particle transport trajectory for each particle.

Bibliography

[1] A. L. Westerling, H. G. Hidalgo, D. R. Cayan and T. W. Swetnam, "Warming and earlier spring increase western US forest wildfire activity," *Science,* vol. 313, no. 5789, pp. 940-943, 2006.

[2] W. G. Bell, "The Great Fire of London in 1666," *Greennwood Publishing Group,* 1971.

[3] E. Koo and P. J. Pagni, "Firebrands and spotting ignition in large-scale fires," *Int. J. Wildland Fire,* vol. 19, no. 7, p. 818, 2010.

[4] W. E. Mell, S. L. Manzello, A. Maranghides, D. Butry and R. G. Rehm, "The wildland-urban interface fire problem-current approaches and research needs," *Int. J. Wildland FIre,* vol. 19, no. 2, pp. 238-251, 2010.

[5] A. Fernandez-Pello, "Wildland fire sppot ignition by sparks and firebrands," vol. 91, pp. 2-10, 2017.

[6] S. D. Tse and A. C. Fernandez-Pello, "On the flight paths of metal particles and embers generated by power lines in high winds-a potential source of wildland fires," *Fire Safety Journal,* vol. 30, no. 4, pp. 333-356, 1998.

[7] S. L. Manzello, "Enabling the Investigation of Structure Vulnerabilities to Wind-Driven Firebrand Showers in Wildland-Urban Interface (WUI) Fires," vol. 11, pp. 83-96, 2014.

[8] S. L. Manzello, A. Maranghides, J. R. Shields and W. E. Mell, "Mass and size distribution of firebrands generated from burning Korean pine (Pinus koraiensis) trees," *Fire Mater.,* vol. 33, pp. 21-31, 2009.

[9] S. L. Manzello, A. Maranghides, W. E. Mell, T. G. Gleary and J. C. Yang, "Firebrand production from burning vegetation," *For. Ecol. Manag,* vol. 234, no. S119, 2006.

[10] S. Manzello, S. Suzuki and M. Gollner, "Role of firebrand combustion in large outdoor fire spread," *Progress in Energy and Combustion Science,* vol. 76, 2020.

[11] S. E. Caton, R. P. Hakes, J. G. Daniel, A. Zhou and M. J. Gollner, "A Review of Pathways to Building Fire Spread in the Wildland Urban Interface Part I: Exposure Conditions," vol. 53, pp. 429-473, 2017.

[12] S. E. Caton, R. P. Hakes, J. G. Daniel, A. Zhou and M. J. Gollner, "A Review of Pathways to Building Fire Spread in the Wildland Urban Interface Part II: Response of Components and Systems and Mitigation Strategies," vol. 53, pp. 475-515, 2017.

[13] A. Tohidi and N. B. Kaye, "The sensitivity of modeled flight distance to the lofting to transport transition criterion in coupled ember flight models," in *Proceedings of the 12th Americas Conference on Wind Engineering*, Seattle, 2013.

[14] C. S. Tarifa, P. Notario and F. G. Moreno, "On the flight paths and lifetimes of burning particles of wood," in *Proceedings of the Symposium (international) on combustion*, 1965.

[15] S. L. Lee and J. M. Hellman, "Firebrand trajectory study using an empirical velocity-dependent burning law," *Combust. Flame,* vol. 15, no. 3, pp. 265-274, 1970.

[16] T. Himoto and K. Tanaka, "Transport of disk-shaped firebrands in a turbulent boundary layer," in *Proceeding of the Eighth International Symposium on Fire Safety Science*, 2005.

[17] A. Tohidi, "Experimental and Numerical Modeling of Wildfire Spread via Fire Spotting (Ph.D. thesis)," 2016.

[18] A. Tohidi and N. B. kaye, "Comprehensive wind tunnel experiments of lofting and downwind transport of non-combusting rod-like model firebrands during firebrand shower scenarios," *Fire Safety Journal,* vol. 90, pp. 95-111, 2017.

[19] Z. Liu, D. Prevatt, L. Aponte-Bermudez, K. Gurley, T. Reinhold and R. Akins, "Field measurement and wind tunnel simulation of hurricane wind loads on a single family dwelling," *Eng. Struct. ,* vol. 31, no. 10, pp. 2265-2274, 2009.

[20] M. L. Albertson, Y. Dai, R. Jensen and H. Rouse, "Diffusion of submerged jets," *Trans. Am. Soc. CIvil. Eng.,* vol. 115, no. 1, pp. 639-664, 1950.

[21] NIST, Fire Dynamics Simulator User's Guide, 6 ed.

[22] A. Tohidi and N. B. Kaye, "Comprehensive wind tunnel experiments of lofting and downwind transport of non-combusting rod-like model firebrands during firebrand shower scenarios," *Fire Safety Journal,* vol. 90, pp. 95-111, 2017.